THE JOURNAL OF PHYSICAL CHEMISTRY Letters

pubs.acs.org/JPCL Letter

Energetic Cost for Being “Redox-Site-Rich” in Pseudocapacitive Energy Storage with Nickel−Aluminum Layered Double Hydroxide Materials

Xianghui Zhang, Cody B. Cockreham, Esra Yılmaz, Gengnan Li, Nan Li, Su Ha, Liangjie Fu, Jianqi Qi, Hongwu Xu, and Di Wu*

Cite This: J. Phys. Chem. Lett. 2020, 11, 3745−3753 Read Online

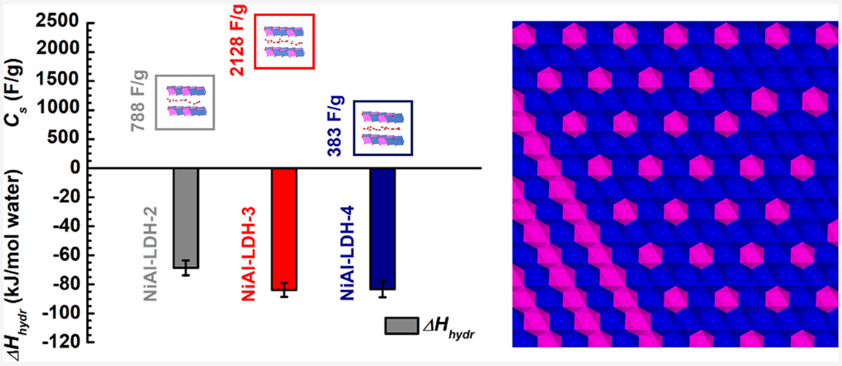

ABSTRACT: Defining the energetic landscape of pseudocapacitive materials such as transition metal layered double hydroxides (LDHs) upon redox-site enrichment is essential to harnessing their power for effective energy storage. Here, coupling acid solution calorimetry, *in situ* XRD, and *in situ* DRIFTS, we demonstrate that as the Ni/Al ratio increases, both as-made (hydrated) and dehydrated NiAl-LDH samples are less stable as evidenced by their enthalpies of formation. Moreover, the higher specific capacity at an intermediate Ni/Al ratio of 3 is enabled by effective water−LDH interactions, which energetically stabilize the excessive near-surface Ni redox sites, solvate intercalated carbonate ions, and fill the expanded vdW gap, paying for the “energetic cost” of being “redox-site-rich”. Thus, from a thermodynamic perspective, engineering molecule/solid−LDH interactions on the nanoscale with confined guest species other than water, which energetically impose stronger stabilization, may help us to achieve their specific capacitance potential.

Electrochemical energy storage devices, primarily batteries and capacitors, are playing critical roles in the ongoing modification of our energy infrastructure.[1−6] Rechargeable battery materials rely on phase transitions and/or solid-state reactions during the charge−discharge processes, while capacitive energy storage mechanisms take advantage of the electrostatic charge storage at or near the surface of the electrode materials.[7−10] Compared with the “endurance athletes”—rechargeable batteries that have high energy density, the advantages of electrochemical capacitors include high power density, long cycle life, and rapid charge−discharge. These properties enable high-performance “sprinter” energy storage devices for short-term charge storage, regenerative braking, and a burst-mode delivery of energy.[11−15]

Depending on the working mechanisms, electrochemical capacitors are typically categorized as (1) electrical double-layer capacitors (EDLCs or supercapacitors) and (2) pseudocapacitors.[11−15] EDLCs rely on the formation of an ionic double layer at the electrode−electrolyte interface for electrical energy storage. Despite their low cost and wide availability, the carbon-based EDLCs suffer from low energy density because of the limitation of surface area and effective interfaces.[16−20] In this regard, pseudocapacitors feature substantially increased energy density accompanied by high power density, rapid charge transfer kinetics, and cycle stability.[21−26] Fundamentally, pseudocapacitive materials store charge at or near their surfaces by reversible redox reactions based on Faradaic charge transfer, in which the concentration of redox sites is a governing factor of the specific capacitance.[22,27,28] Thus, understanding the impacts of redox-site concentration on the phase stability, structure, and storage

Received: March 19, 2020
Accepted: April 22, 2020
Published: April 22, 2020

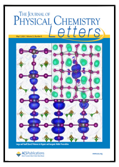

https://dx.doi.org/10.1021/acs.jpclett.0c00865
J. Phys. Chem. Lett. 2020, 11, 3745−3753

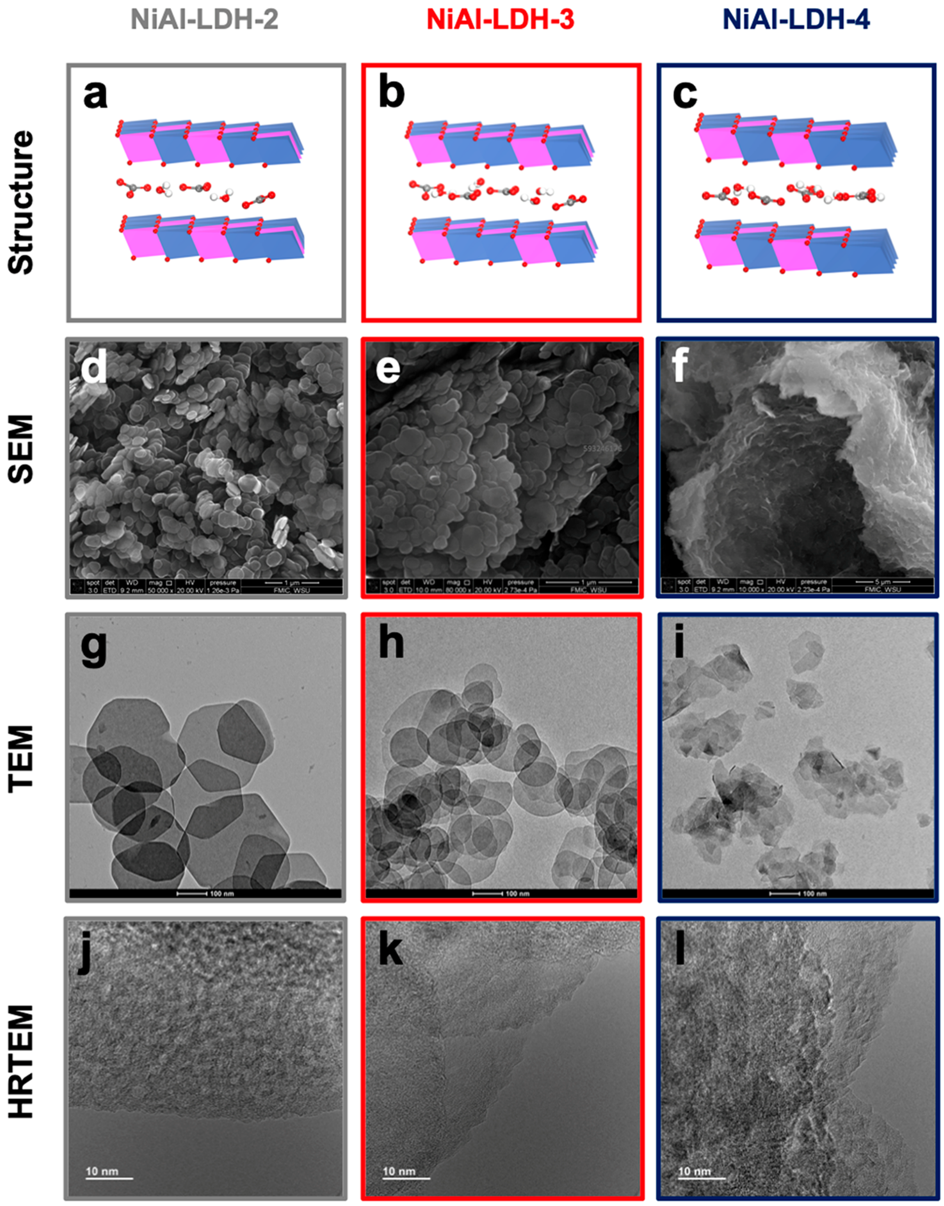

Figure 1. Illustrated structures (a−c) and morphologies of NiAl-LDH samples revealed by scanning electron microscopy (SEM, d−f), transmission electron microscopy (TEM, g−i), and high-resolution transmission electron microscopy (HRTEM, j−l). NiAl-LDH-2 (gray), NiAl-LDH-3 (red), and NiAl-LDH-4 (navy).

of pseudocapacitive materials, such as transition metal oxides,[22,25,26] hydroxides,[12,13] and sulfides[29,30] along with conductive polymers,[31] is essential for further materials discovery, rational design, and optimization.

This paper elucidates the energetics−structure−performance relationships of transition metal layered double hydroxides (TM-LDHs) as the redox-site concentration is tuned. TM-LDHs possess positively charged brucite-like metal hydroxide layers constructed by M^{2+} and M^{3+} transition metal octahedra.[32] Introduction of trivalent cations M^{3+} into the $M^{2+}(OH^-)_2$ layer leads to layer-possessed positive charges and simultaneous intercalation of charge-balancing anions (A^{n-}) confined within the interlayer space, which is also filled by neutrally charged guest species, such as water molecules.[12,33] The open two-dimensional (2D) structure of TM-LDHs enables highly efficient Faradaic redox reactions at the near-surface transition metal sites with fast kinetics. In an earlier study of NiAl-LDH with CO_3^{2-} as the charge-balancing anions, we demonstrate that an increase in the Ni/Al ratio from 2 to 4 leads to an increased Ni redox-site concentration, expanded van der Waals (vdW) gap resulting in faster charge transport kinetics, and a degraded near-surface crystallinity.[21] We also find that the pseudocapacitive charge storage capacity is not positively correlated to the Ni/Al ratio. Additionally, a high near-surface crystallinity is crucial to ensure a high pseudocapacitive capacitance.[21,22,25] However, the thermodynamic mechanisms for the complex interplay among the Ni redox-site concentration, near-surface crystallinity, and intercalation chemistry of NiAl-LDHs have not been clearly and quantitatively identified from microscopic and macroscopic perspectives.

Here, we report a systematic study that elucidates the impacts of Ni content on the energetic stability and thermodynamics−structure−performance relationship of

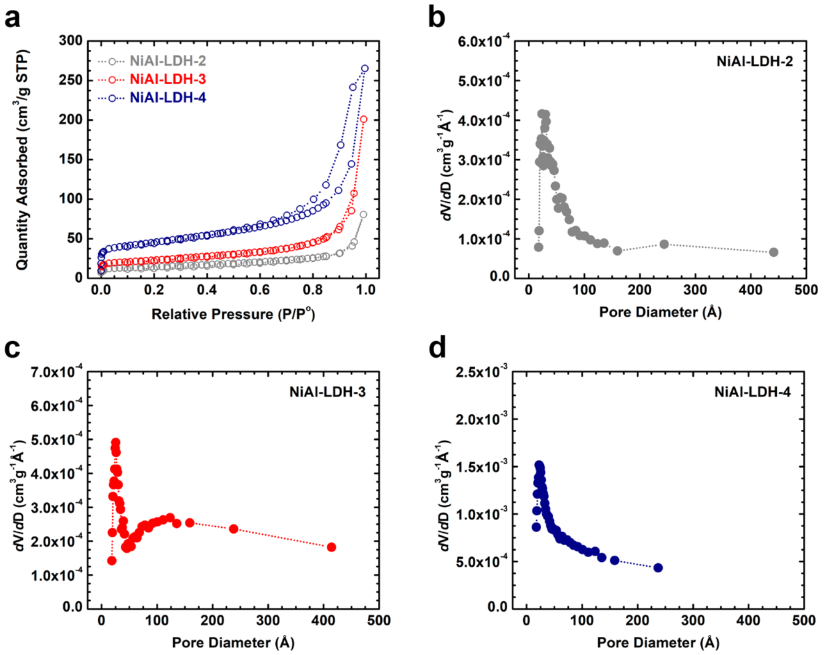

Figure 2. (a) Nitrogen adsorption and desorption full isotherms at −196 °C, and pore size distribution of (b) NiAl-LDH-2, (c) NiAl-LDH-3, and (d) NiAl-LDH-4.

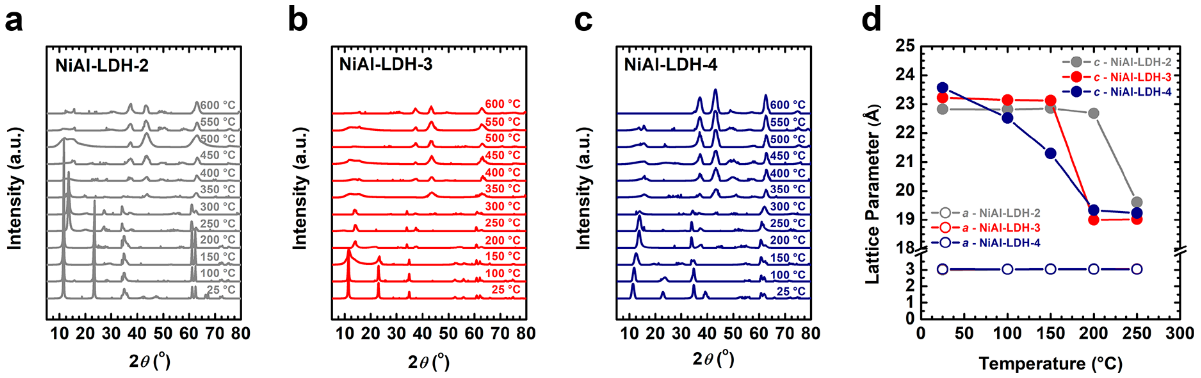

Figure 3. *In situ* X-ray diffraction (XRD) patterns of all samples as a function of temperature from 25 to 600 °C at 10 °C/min under a helium flow of 30 mL/min with a hold time of 5 min at each temperature prior to measurement. Data were collected from 5 to 80°. (a) NiAl-LDH-2, (b) NiAl-LDH-3, and (c) NiAl-LDH-4. (d) Lattice parameters of all NiAl-LDH samples as a function of temperature. Note, the *a* parameters of all three NiAl-LDH samples overlap each other due to the similarity in their intraplanar crystallinity.

NiAl-LDH by integrating two powerful *in situ* techniques, *in situ* X-ray diffraction (XRD) and *in situ* diffuse reflectance infrared Fourier transform spectroscopy (DRIFTS), with a unique calorimetric method, near-room-temperature acid solution calorimetry. The obtained results suggest that Ni enrichment leads to decreased energetic, thermal, structural, and morphological stability for both as-made (hydrated) and dehydrated NiAl-LDHs. Further, we demonstrate that the intercalated (2D-confined) water molecules substantially neutralize the significant metastability introduced by Ni redox-site enrichment, and the optimized specific capacitance is the result of the subtle balance between the energetic stability of LDH layers and water−layer guest−host interactions. This work also highlights the power of integrating *in situ* structural, spectroscopic, and thermodynamic techniques to unravel fundamental mechanisms underlying the properties and behavior of energy storage materials at application conditions.

Composition, Morphology, Structure, and Surface Analyses. The compositions of all samples are listed in Table S1. The illustrated structures and electron microscopy images are presented in Figure 1. As seen from the scanning electron microscopy (SEM) and transmission electron microscopy (TEM) images, NiAl-LDH-2 possesses a hexagonal platelet nanosheet morphology, while the shape of NiAl-LDH-3 and -4 platelet nanosheets appear to lack well-defined geometry. Investigated by high resolution transmission electron microscopy (HRTEM), NiAl-LDH-4 appears nearly amorphous at atomic scales in the interplanar direction with many jagged grain boundary defects near the layer edges. By contrast, NiAl-LDH-2 and NiAl-LDH-3 appear to have better near-surface crystallinity than NiAl-LDH-4 with smooth rounded layer edges. As the Ni/Al ratio increases, the particle size decreases from ∼250 nm for NiAl-LDH-2 to ∼80 nm for NiAl-LDH-4. The N_2 adsorption and desorption full isotherm analysis data are plotted in Figure 2 and summarized in Table S1. The specific surface area increases as the Ni/Al ratio increases.

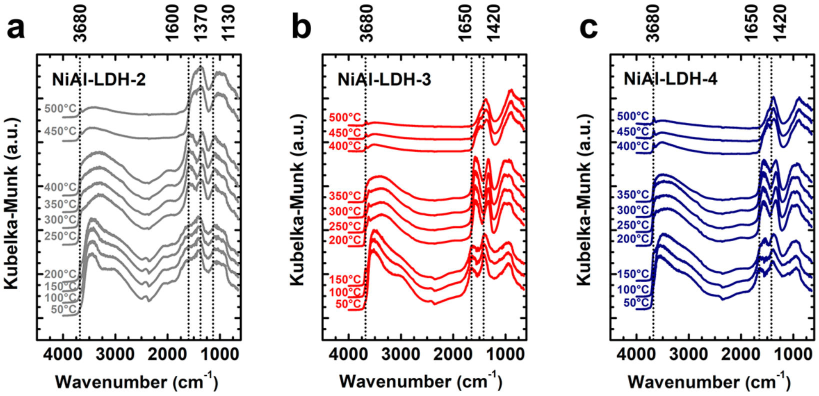

Figure 4. *In situ* diffuse reflectance infrared Fourier transform spectroscopy (DRIFTS) spectra of each sample as a function of temperature from 50 to 500 °C under a helium flow of 50 mL/min: (a) NiAl-LDH-2, (b) NiAl-LDH-3, and (c) NiAl-LDH-4.

Specifically, the BET specific areas are 47.5, 77.0, and 152.1 m^2/g for NiAl-LDH-2, -3, and -4, respectively. This trend is consistent with the particle size decrease observed in the electron microscopy analyses. In addition, in BJH pore size analysis, NiAl-LDH-3 presents the largest pore size of 22.3 nm, while NiAl-LDH-4 has the smallest mesoscale porosity of 8.0 nm. The pore dimension of NiAl-LDH-2 is 15.8 nm. In general, Ni enrichment leads to decreased particle size, degraded morphology, and increased surface area.

Structural Evolutions. In situ XRD patterns for NiAl-LDH samples are presented in Figure 3a−c. All samples exhibit hydrotalcite-like structures representative of metal hydroxide layered structures (PDF# 15-0087, also see Figure S1). Generally, before eventual degradation as the temperature increases, the representative peaks of each NiAl-LDH broaden and shift to higher 2θs. Phase transition due to degradation of the brucite-like metal hydroxide layered structure was observed at above 300 °C for NiAl-LDH-2 and -3 and 250 °C for NiAl-LDH-4. At temperatures higher than 400 °C, each sample decomposes to a mixed phase of NiO and Al_2O_3, shown in Figure S2. Lattice parameters of the NiAl-LDHs in hexagonal close packing found from representative peaks of (003) and (110) are presented as a function of temperature in Figure 3d. The *a* lattice parameter, which represents the cell dimension parallel to the brucite-like layer, does not change appreciably throughout the temperature range investigated. Seen in our previous work and repeated here, the *c* lattice parameter (related to the *d*-spacing by the equation $c = 3 \times d_{003}$) at 25 °C, which represents the cell dimension in the interlayer direction, increases with Ni content.[21] As Ni content increases and Al content decreases, the total positive charge of the metal hydroxide layer lessens; proportionately, interlayer charge-balancing anions decrease limiting electrostatic interactions.[21] As temperature increases, the *c* lattice parameter of each sample decreases. The *c* lattice parameters exhibit a 3−4 Å relatively abrupt decrease from 200 to 250 °C for NiAl-LDH-2, and from 150 to 200 °C for NiAl-LDH-3. Such a stepwise decrease is indicative of the loss of one layer of intercalated water (dehydration), since interlayer-confined water molecules are ~2.5 Å in size.[34] Interestingly, NiAl-LDH-3 seemingly expands its interlayer distance from 250 to 300 °C. We attribute this to normal lattice thermal expansion or an artifact from the growing disorder in stacking, while carbonate deintercalates, and subsequent structural degradation is observed from the wide distribution of the (003) peak at 300 °C (see Figure 3b). The *c* parameter of NiAl-LDH-4 features a much more gradual decrease for ~4 Å spanning from 25 to 200 °C, presumably due to more chaotic stacking (seen in SEM and/or TEM) leading to varied interlayer environments. As Ni content increases, interlayer dehydration occurs at lower temperatures. In summary, the *in situ* XRD results strongly highlights (1) the loss of interlayer space after dehydration of intercalated water, and (2) phase transition to oxide phases at temperature above 400 °C, which is accompanied by a release of CO_2 (see the TG-DSC-MS data plotted in Figure S3).[21]

Interfacial Phenomena. The *in situ* DRIFTS spectra suggest all NiAl-LDH samples share three vibrational features (see Figure 4), including (1) a broad absorption spanning from 4000 to 2500 cm^{-1} owing to the O−H stretching vibration of hydroxyl groups from the brucite-like layers and intercalated water molecules; (2) three overlapped peaks between 2000 and 650 cm^{-1} due to interlayer-confined H_2O and carbonate species and surface OH groups, specifically, one at ~1650 cm^{-1} (bending vibration of adsorbed water) and two between 1370 and 1000 cm^{-1} (asymmetric stretching of interlayer carbonate species); (3) several relatively weak absorption peaks between 1000 and 650 cm^{-1} belonging to a lattice vibration of the metal−oxygen bonds within the NiAl-LDH layer.

Both *in situ* DRIFTS and TG-DSC-MS results strongly suggest a *two-stage mechanism* for thermal degradation of NiAl-LDH. Specifically, in ***Stage I***, interlayer dehydration (from 25 to ~200 °C), starting from ~150 °C, a sharp peak at 3680 cm^{-1} appears, which is assigned to the ν(OH) of isolated surface hydroxyl groups of LDH.[35] Interestingly, although this peak is clearly well-resolved for NiAl-LDH-2 and -3, it appears to be broad and nearly undetectable during ***Stage I*** dehydration of NiAl-LDH-4. Dehydration in ***Stage I*** leads to removal of intercalated water molecules, reducing the hydrogen bonding among interlayer adsorbed/confined species. As temperature increases, the low wavenumber peaks of NiAl-LDH-2 become better resolved, splitting into three sharp peaks centered at 1600, 1370, and 1130 cm^{-1}. For NiAl-LDH-3 and -4, shifts from 1650 to 1600 and from 1420 to 1370 cm^{-1} were observed. The signal at ~1600 cm^{-1} is attributed to the bending mode of exposed surface OH groups from $Ni(OH)_2$ and $Al(OH)_3$.[36] Hence, a right-shift from 1650 to 1600 cm^{-1} is caused by dehydration of layer-confined water molecules. A right-shift of the peak at 1420 cm^{-1} due to a ν(C−O) of carbonate anions arises from significantly enhanced anion−layer interactions after dehydration.[35] Interestingly, all post

Stage I dehydration samples present similar DRIFTS spectra. This is because removal of water molecules from the interlayer space significantly reduces the chemical complexity of guest−host interactions among various intercalated (confined) species (mainly carbonates) and the NiAl-LDH layers. After complete interlayer dehydration, the high wavenumber broad peak spanning from 4000 to 2500 cm^{-1} becomes near-absent. The remaining peaks are mainly from the layer-possessed functional groups and charge-balancing carbonates.

Stage II degradation of the LDH structure from ∼200 °C concludes at ∼450 °C for NiAl-LDH-2 and at about 400 °C for NiAl-LDH-3 and -4, in which two significant transitions are detected by *in situ* DRIFTS. Specifically, the intensity of peak at 1370 cm^{-1} decreases as temperature increases, which strongly suggests decomposition of interlayer-confined carbonate species to CO_2 that was also seen within the same temperature range in the TG-DSC-MS thermal analyses.[33,34] Meanwhile, the peak at ∼1600 cm^{-1} completely disappears. According to the *in situ* XRD data, this is caused by thermal decomposition of $Ni(OH)_2$ and $Al(OH)_3$ and phase transition to NiO and Al_2O_3 (see Figures 3 and S2). This set of *in situ* DRIFTS data is in excellent agreement with TG-DSC-MS and *in situ* XRD results, which reveal a *two-stage degradation mechanism*, including ***Stage I*** interlayer dehydration leading to the loss of the interlayer gallery and ***Stage II*** degradation of LDH layers with a significant phase transition of all NiAl-LDH samples induced by the decomposition of the anionic charge-balancing carbonate species.

Energetics of As-Made and Dehydrated NiAl-LDHs. According to the TG-DSC-MS thermal analysis results, the integral enthalpies of hydration (ΔH_{hydr}) of NiAl-LDH samples are −68.68 ± 5.12, −83.80 ± 4.81, and −83.32 ± 5.53 kJ/mol of water, for NiAl-LDH-2, -3, and -4, respectively. The directly measured enthalpies of dissolution of all samples in HCl aqueous solution (5 N) at 40 °C are listed in Table S2. The enthalpies of formation, ΔH_{f}, for NiAl-LDH samples from NiO, γ-$Al(OH)_3$, H_2O, and CO_2, are calculated using the thermodynamic cycle listed in Table S3. In general, formation of the as-made fully hydrated NiAl-LDHs is energetically favorable, reflected by the negative formation enthalpy (ΔH_{f}) values. ΔH_{f} tends to be less exothermic as the Ni/Al ratio or interlayer spacing increases, ranging from −59.00 ± 1.46 to −37.80 ± 5.37 kJ/mol of Ni (see Figure 5). Further, with the enthalpies of formation and dehydration, we are able to calculate the formation enthalpies of dehydrated NiAl-LDH samples with the interlayer-confined water removed, $\Delta H_{\mathrm{f\text{-}dehy}}$. Surprisingly, all $\Delta H_{\mathrm{f\text{-}dehy}}$ values are positive, strongly suggesting the dehydrated NiAl-LDH samples are energetically unfavorable. Moreover, $\Delta H_{\mathrm{f\text{-}dehy}}$ becomes more endothermic as the Ni/Al ratio increases. Specifically, the $\Delta H_{\mathrm{f\text{-}dehy}}$ values are 19.95 ± 6.06, 31.50 ± 7.36, and 35.26 ± 7.24 kJ/mol of Ni for NiAl-LDH-2, -3, and -4, respectively (see Figure 5). Table S4 lists all calorimetric data discussed above. All data are presented with error bars.

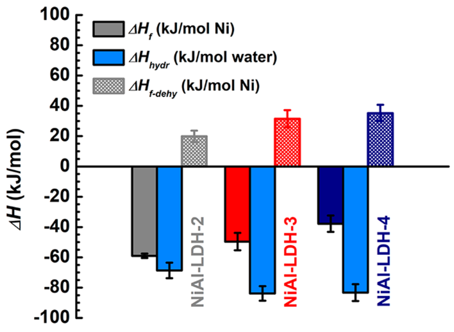

Figure 5. Enthalpies of formation from NiO (s), $Al(OH)_3$ (s), H_2O (l), and CO_2 (g) at 25 °C for all NiAl-LDH samples.

Energetic Landscape of NiAl-LDH, Critical Role of Water Intercalation, and Structure−Energetics−Performance Relationships. Our earlier study demonstrated that an increase in the Ni/Al ratio leads to (1) an increase of the Ni redox-site concentration, (2) expansion of interlayer space (van der Waals gap), (3) degradation of crystallinity and morphology (see Figures 1 and 3), (4) enhancement of ion transport kinetics, and (5) modification of specific capacitance (F/g) with the highest capacity recorded for NiAl-LDH-3.[33] All these trends are summarized in Figure 6. Using *in situ* methodologies and from a thermodynamic perspective, our present study leads to the following general conclusions: *first*, as the Ni content increases, both as-made (hydrated) and dehydrated NiAl-LDHs tend to be energetically less stable, and all dehydrated NiAl-LDH samples are no longer stable, reflected by the positive formation enthalpies ($\Delta H_{\mathrm{f\text{-}dehy}}$). Although decreased stability upon introduction of more redox defects is a common phenomenon seen for solid-state oxide and hydroxide materials,[37−39] the endothermic enthalpies of formation for dehydrated NiAl-LDH are not typically seen, which indicates that upon removal of the intercalated water, the NiAl-LDH is unstable and will readily transform to more energetically favorable phases. Hence, interlayer-confined species such as small molecules, ions, and/or materials are essential to minimize or neutralize the metastability generated by redox-site enrichment. In other words, interlayer-confined species pay the "cost of being redox-site-rich". *Second*, hydration plays critical thermodynamic roles in determination of the functionality of NiAl-LDH structures by (i) energetically maintaining the open interlayer gallery structure for electrolyte intercalation with rapid kinetics; (ii) stabilizing the interlayer-confined charge-balancing carbonates by acting as solvents; and (iii) minimizing the metastability generated by highly concentrated layer-possessed hydroxyls in NiAl-LDHs. The energetic balance through subtle interplay between compositional factors and water−layer guest−host interactions governs the specific capacitance of NiAl-LDH materials (see Figure 7). *Lastly*, inspired by the thermodynamic insights into NiAl-LDH formation and hydration obtained here, we anticipate that we will be able to pay the "energetic cost of being redox-site-rich" by interfacial engineering strategies to tune the chemical nature and magnitudes of guest−host interactions to synthesize pseudocapacitive energy storage materials with enhanced stability, faster kinetics, and higher capacitance. Also, we expect that by tuning the degree of hydration, we may manipulate the kinetics, energetics, and capacitance of TM-LDH materials to engineer desired qualities.

In our earlier study, we have shown that Ni atom enrichment for NiAl-LDH leads to an expansion in interlayer spacing facilitating faster kinetics and an increased number of energy storage sites during the reversible charge−discharge process. Here, from a thermodynamic perspective, we further the fundamental understanding of the NiAl-LDH system by demonstrating that the increase in Ni redox-site concentration results in decreased energetic stability for both as-made (hydrated) and dehydrated NiAl-LDHs, reflected by their

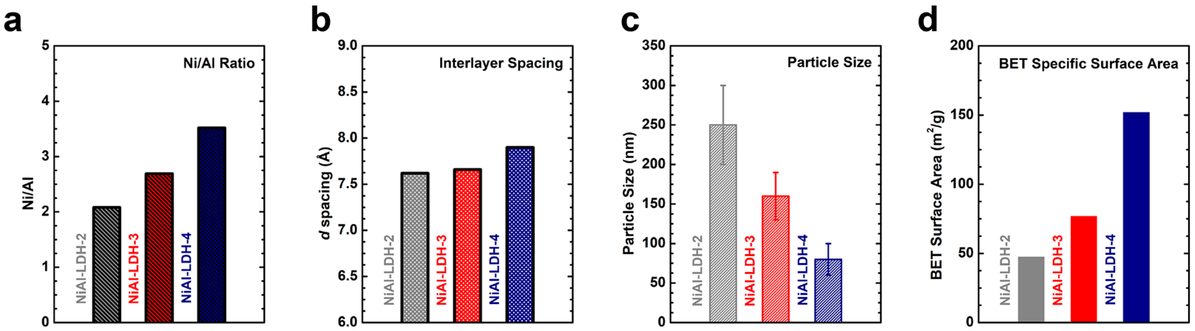

Figure 6. (a) Ni/Al ratio, (b) *d*-spacing reflecting interlayer spacing, (c) particle size for all NiAl-LDH samples, and (d) Brunauer−Emmett−Teller (BET) specific areas.[21]

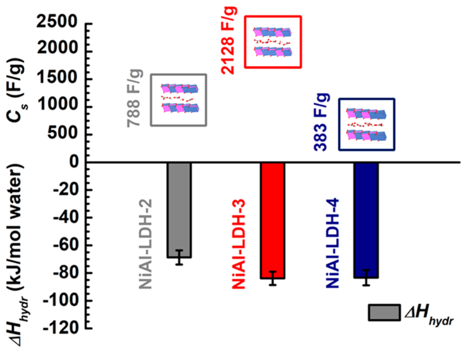

Figure 7. Energetic−structure−performance relationships for all NiAl-LDHs with Ni/Al ratios from 2 to 4. The specific capacity (C_s) values were reported in our earlier paper.[21]

enthalpies of formation. Moreover, interlayer hydration significantly stabilizes the metastability introduced by Ni enrichment. The highest specific capacity observed for NiAl-LDH-3 (2128 F/g at 1 A/g) with an intermediate Ni content is achieved by effective stabilization from hydration through subtly balanced interlayer confinement (intercalation) and interfacial binding, which intrinsically pay the "energetic cost" generated by the increase of the Ni/Al ratio. Therefore, our study highlights the critical role of hydration and demonstrates that interfacial engineering on the nanoscale within the interlayer space is a promising strategy to fine-tune the confinement chemistry and surface redox sites for substantial enhancement of the energy storage properties of transition metal layered double hydroxides (TM-LDHs).

■ EXPERIMENTAL METHODS

Materials Synthesis. All chemicals used were Sigma-Aldrich ACS reagent grade. NiAl-LDH samples were prepared hydrothermally using a Teflon-lined autoclave. Each sample was denoted as NiAl-LDH-*n* according to the Ni/Al ratio (*n*). Specifically, $Ni(NO_3)_2{\cdot}6H_2O$ (purity > 98.5%) and $Al(NO_3)_3{\cdot}9H_2O$ (purity > 98%) (Ni/Al = *n* and Ni + Al = 1.875 mmol) were dissolved in 25 mL of nanopure water (18.2 MΩ·cm). For NiAl-LDH-2, $Ni(NO_3)_2{\cdot}6H_2O$ (purity > 98.5%) and $Al(NO_3)_3{\cdot}9H_2O$ (purity > 98%) were 1.25 and 0.625 mmol, respectively. For NiAl-LDH-3, $Ni(NO_3)_2{\cdot}6H_2O$ (purity > 98.5%) and $Al(NO_3)_3{\cdot}9H_2O$ (purity > 98%) were 1.460 and 0.456 mmol, respectively. For NiAl-LDH-4, $Ni(NO_3)_2{\cdot}6H_2O$ (purity > 98.5%) and $Al(NO_3)_3{\cdot}9H_2O$ (purity > 98%) were 1.25 and 0.365 mmol, respectively. In addition, the precipitant used was hexamethylenetetramine (HMT, 2.20 mmol, purity > 99%) for NiAl-LDH-2, and urea (4.13 mmol, purity > 99%) was applied to precipitate NiAl-LDH-3 and -4. In each synthesis, the mixture was introduced into a 50 mL Teflon-lined autoclave for the hydrothermal reaction at 180 °C for 72 h. The precipitates were filtered and washed with nanopure water (18.2 MΩ·cm) followed by drying under vacuum at room temperature.[21]

Ex Situ Powder X-ray Diffraction (XRD), Compositional, and Thermal Analyses. For phase identification, room temperature *ex situ* powder X-ray diffraction (XRD) patterns of the synthesized NiAl-LDH samples were collected with a Rigaku Miniflex 600 diffractometer (40 kV, 15 mA with Cu Kα radiation, λ = 0.15418 nm). Data were recorded between 5 and 80° at 1°/min. Compositional and thermal analyses were performed in our earlier study.[21] The chemical compositions of all samples were characterized using inductively coupled plasma mass spectrometry (ICP-MS, Agilent 770). The TG-DSC-MS thermal analyses were carried out on a Netzsch Instrument STA 449 F5 Jupiter coupled to a QMS 403 D Aëolos quadrupole mass spectrometer in our earlier study, emphasizing energy storage performance. The accuracy of enthalpy from DSC using the STA 449 F5 Jupiter is ±2% for most materials. In each measurement, about 20 mg of sample was analyzed in a platinum crucible from 30 to 1000 °C at 10 °C/min under N_2 flow (60 mL/min). Evolved gases of TG-DSC experiments were identified simultaneously by the coupled MS including m/z = 18 (H_2O) and 44 (CO_2). The DSC data were also used to calculate the dehydration enthalpy of each NiAl-LDH sample. The *ex situ* XRD, ICP-MS, and TG-DSC-MS data have been reported in our earlier study on the same set of NiAl-LDH samples[21] (see Table S1 and Figures S1 and S3).

N_2 Adsorption and Desorption Full Isotherm Analysis. The Brunauer−Emmett−Teller (BET) and Barrett, Joyner, and Halenda (BJH) surface area and pore size distribution analyses were carried out using N_2 adsorption and desorption full isotherm analysis at −196 °C (77 K) on a Micromeritics 3Flex gas adsorption analyzer. Before each measurement, the sample was degassed *in situ* at the analysis port at 250 °C for 2 h.

Electron Microscopy (EM). We examined the sample morphology using scanning electron microscopy (SEM, Quanta 200F), transmission electron microscopy (TEM, FEI Tecnai T20 with a LaB_6 cathode at 200 kV) in the Franceschi Microscopy and Imaging Center at Washington State University, and high-resolution transmission electron microscopy (HRTEM, FEI Titan 80-300 TM with a monochromator, image aberration corrector, and a PHENIX energy dispersive X-ray spectrometer detector) at Los Alamos National Laboratory. *ImageJ* (NIH) was employed for micrograph analysis.[40] The SEM specimen was prepared by loading the sample on carbon tape, which was placed on an aluminum stub. The specimen for TEM and HRTEM analyses was prepared by dispersing a small amount of sample powder in ethanol using ultrasonication. Subsequently, several drops of suspension were dried on 200 mesh carbon-coated nickel grid (TEM) and a 200 mesh carbon-coated copper grid (HRTEM).

In Situ X-ray Diffraction (In Situ XRD). The structural evolution of all NiAl-LDH samples as temperature increases from room temperature to 600 °C was monitored by *in situ* powder X-ray diffraction (*in situ* XRD). The data were obtained using a Rigaku Smartlab X-ray diffractometer with Cu Kα radiation (λ = 1.5406 Å) coupled with a platinum strip heater operated at a scan rate of 4°/min in the 2θ range of 5−80° with a heating rate of 10 °C/min under 30 mL/min of helium with a hold time of 5 min prior to each scan. *d*-Spacing was calculated using Bragg's law. The lattice parameters and unit cell volume of each sample were calculated. PDF database references were used to identify the phases of hydrotalcite (naturally occurring $Mg_6Al_2(OH)_{16}CO_3 \cdot 4H_2O$), PDF# 00-014-0191, NiO, PDF# 01-073-1519, and Al_2O_3, PDF# 01-073-5928.

In Situ Diffuse Reflectance Infrared Fourier Transform Spectroscopy (In Situ DRIFTS). *In situ* diffuse reflectance infrared Fourier transform spectroscopy (*in situ* DRIFTS) analysis was carried out in a high-temperature cell (Spectra-Tech) equipped with ZnSe windows (IR transparent). Prior to each analysis, the sample was finely ground and placed in a ceramic crucible. The spectra were recorded from room temperature to 500 °C under helium flow (50 mL/min). The background spectra were collected under the same conditions. We were not able to reach as high as 600 °C as we did in the *in situ* XRD experiments due to instrumental limitations.

Near-Room-Temperature Acid Solution Calorimetry. Near-room-temperature acid solution calorimetry using a Setaram C80 microcalorimeter with 5 mol/L of hydrochloric acid (HCl) from Sigma-Aldrich was employed to measure the enthalpies of dissolution to derive the NiAl-LDH formation enthalpies. The Setaram C80 microcalorimeter employed has a sensitivity (Joule effect at 30 °C) of 30 μW/mW with a temperature accuracy of ±0.1% and an enthalpy accuracy of ±1%. In a typical measurement, a loose, hand-pressed sample pellet (~4 mg) was dropped into the HCl solution (10 mL) kept at 40 °C. The slightly elevated temperature aided rapid dissolution of NiAl-LDH pellet, which led to a calorimetric peak. A similar strategy was also applied in an earlier study on porous silica using hydrofluoric acid solution calorimetry at 50 °C, in which the temperature effects were negligible.[41,42] Complete sample dissolution was confirmed by the return to a flat baseline. Integration of the area under each calorimetric peak returned the heat of dissolution (kJ) for each pellet. At least four successful measurements were performed on each sample to ensure reproducibility. The error bars were calculated as two standard deviations of the mean. KCl (NIST) dissolution was used to calibrate the microcalorimeter.

■ ASSOCIATED CONTENT

Supporting Information

The Supporting Information is available free of charge at https://pubs.acs.org/doi/10.1021/acs.jpclett.0c00865.

> Additional compositional and structural information, surface area, raw calorimetric data, thermodynamic cycle, enthalpies of dissolution, formation, and hydration, additional *ex situ* and *in situ* XRD patterns, and TG-DSC-MS results (PDF)

■ AUTHOR INFORMATION

Corresponding Author

Di Wu − *Alexandra Navrotsky Institute for Experimental Thermodynamics, The Gene and Linda Voiland School of Chemical Engineering and Bioengineering, Department of Chemistry, and Materials Science and Engineering, Washington State University, Pullman, Washington 99163, United States;* orcid.org/0000-0001-6879-321X; Email: d.wu@wsu.edu

Authors

Xianghui Zhang − *Alexandra Navrotsky Institute for Experimental Thermodynamics and The Gene and Linda Voiland School of Chemical Engineering and Bioengineering, Washington State University, Pullman, Washington 99163, United States*

Cody B. Cockreham − *Alexandra Navrotsky Institute for Experimental Thermodynamics and The Gene and Linda Voiland School of Chemical Engineering and Bioengineering, Washington State University, Pullman, Washington 99163, United States; Earth and Environmental Sciences Division, Los Alamos National Laboratory, Los Alamos, New Mexico 87545, United States*

Esra Yılmaz − *Alexandra Navrotsky Institute for Experimental Thermodynamics and The Gene and Linda Voiland School of Chemical Engineering and Bioengineering, Washington State University, Pullman, Washington 99163, United States; Department of Chemical Engineering, Ege University, Izumir 35100, Turkey;* orcid.org/0000-0001-5217-5425

Gengnan Li − *Alexandra Navrotsky Institute for Experimental Thermodynamics and The Gene and Linda Voiland School of Chemical Engineering and Bioengineering, Washington State University, Pullman, Washington 99163, United States*

Nan Li − *Center for Integrated Nanotechnologies, Los Alamos National Laboratory, Los Alamos, New Mexico 87545, United States*

Su Ha − *The Gene and Linda Voiland School of Chemical Engineering and Bioengineering, Washington State University, Pullman, Washington 99163, United States*

Liangjie Fu − *Centre for Mineral Materials, School of Minerals Processing and Bioengineering, Central South University, Changsha, Hunan 410083, China*

Jianqi Qi − *College of Physics, Sichuan University, Chengdu 610064, China;* orcid.org/0000-0002-6884-1258

Hongwu Xu − *Earth and Environmental Sciences Division, Los Alamos National Laboratory, Los Alamos, New Mexico 87545, United States*

Complete contact information is available at: https://pubs.acs.org/10.1021/acs.jpclett.0c00865

Notes

The authors declare no competing financial interest.

■ ACKNOWLEDGMENTS

This work was supported by institutional funds from the Gene and Linda Voiland School of Chemical Engineering and Bioengineering and fund of the Alexandra Navrotsky Institute for Experimental Thermodynamics at Washington State University. X.Z. is supported by the Chambroad Distinguished

Fellowship. C.B.C. received support from the Achievement Rewards for College Scientists (ARCS) Fellowship from the ARCS Seattle Chapter. This work was performed, in part, at the Center for Integrated Nanotechnologies, an Office of Science User Facility operated for the U.S. Department of Energy (DOE) Office of Science. Los Alamos National Laboratory, an affirmative action equal opportunity employer, is managed by Triad National Security, LLC for the U.S. Department of Energy's NNSA, under contract 89233218CNA000001.

■ REFERENCES

(1) Jiang, H.; Lee, P. S.; Li, C. 3D Carbon Based Nanostructures for Advanced Supercapacitors. *Energy Environ. Sci.* **2013**, *6*, 41.

(2) Pushparaj, V. L.; Shaijumon, M. M.; Kumar, A.; Murugesan, S.; Ci, L.; Vajtai, R.; Linhardt, R. J.; Nalamasu, O.; Ajayan, P. M. Flexible Energy Storage Devices Based on Nanocomposite Paper. *Proc. Natl. Acad. Sci. U. S. A.* **2007**, *104*, 13574.

(3) Wu, X. L.; Jiang, L. Y.; Cao, F. F.; Guo, Y. G.; Wan, L. J. LiFePO4 Nanoparticles Embedded in a Nanoporous Carbon Matrix: Superior Cathode Material for Electrochemical Energy-Storage Devices. *Adv. Mater.* **2009**, *21*, 2710.

(4) Liu, R.; Lee, S. B. MnO2/Poly(3,4-Ethylenedioxythiophene) Coaxial Nanowires by One-Step Coelectrodeposition for Electrochemical Energy Storage. *J. Am. Chem. Soc.* **2008**, *130*, 2942.

(5) Mai, L.; Tian, X.; Xu, X.; Chang, L.; Xu, L. Nanowire Electrodes for Electrochemical Energy Storage Devices. *Chem. Rev.* **2014**, *114*, 11828.

(6) Chen, K.; Song, S.; Liu, F.; Xue, D. Structural Design of Graphene for Use in Electrochemical Energy Storage Devices. *Chem. Soc. Rev.* **2015**, *44*, 6230−6257.

(7) Yin, Y.; Zhang, H.; Wu, P.; Zhou, B.; Cai, C. Iron Phosphate Nanostructures Synthesized by Microwave Method and Their Applications in Biosensing. *Nanotechnology* **2010**, *21* (42), 425504.

(8) Armand, M.; Tarascon, J. M. Building Better Batteries. *Nature* **2008**, *451*, 652.

(9) Arico, A. S.; Bruce, P.; Scrosati, B.; Tarascon, J.-M.; van Schalkwijk, W. Nanostructured Materials for Advanced Energy Conversion and Storage Devices. *Nat. Mater.* **2005**, *4* (5), 366−377.

(10) Dominko, R.; Bele, M.; Goupil, J. M.; Gaberscek, M.; Hanzel, D.; Arcon, I.; Jamnik, J. Wired Porous Cathode Materials: A Novel Concept for Synthesis of LiFePO4. *Chem. Mater.* **2007**, *19*, 2960.

(11) Chen, H.; Hu, L.; Chen, M.; Yan, Y.; Wu, L. Nickel-Cobalt Layered Double Hydroxide Nanosheets for High-Performance Supercapacitor Electrode Materials. *Adv. Funct. Mater.* **2014**, *24* (7), 934−942.

(12) Zhao, J.; Chen, J.; Xu, S.; Shao, M.; Zhang, Q.; Wei, F.; Ma, J.; Wei, M.; Evans, D. G.; Duan, X. Hierarchical NiMn Layered Double Hydroxide/Carbon Nanotubes Architecture with Superb Energy Density for Flexible Supercapacitors. *Adv. Funct. Mater.* **2014**, *24*, 2938.

(13) Zhao, M.; Zhao, Q.; Li, B.; Xue, H.; Pang, H.; Chen, C. Recent Progress in Layered Double Hydroxide Based Materials for Electrochemical Capacitors: Design, Synthesis and Performance. *Nanoscale* **2017**, *9*, 15206.

(14) Salunkhe, R. R.; Tang, J.; Kamachi, Y.; Nakato, T.; Kim, J. H.; Yamauchi, Y. Asymmetric Supercapacitors Using 3D Nanoporous Carbon and Cobalt Oxide Electrodes Synthesized from a Single Metal-Organic Framework. *ACS Nano* **2015**, *9*, 6288.

(15) Moosavifard, S. E.; El-Kady, M. F.; Rahmanifar, M. S.; Kaner, R. B.; Mousavi, M. F. Designing 3D Highly Ordered Nanoporous CuO Electrodes for High-Performance Asymmetric Supercapacitors. *ACS Appl. Mater. Interfaces* **2015**, *7*, 4851.

(16) Miller, J. R.; Simon, P. Electrochemical Capacitors for Energy Management. *Science* **2008**, *321*, 651.

(17) Burke, A. Ultracapacitors: Why, How, and Where Is the Technology. *J. Power Sources* **2000**, *91* (1), 37−50.

(18) Giri, S.; Ghosh, D.; Das, C. K. Growth of Vertically Aligned Tunable Polyaniline on Graphene/ZrO 2 Nanocomposites for Supercapacitor Energy-Storage Application. *Adv. Funct. Mater.* **2014**, *24*, 1312.

(19) Chen, L. F.; Zhang, X. D.; Liang, H. W.; Kong, M.; Guan, Q. F.; Chen, P.; Wu, Z. Y.; Yu, S. H. Synthesis of Nitrogen-Doped Porous Carbon Nanofibers as an Efficient Electrode Material for Supercapacitors. *ACS Nano* **2012**, *6*, 7092.

(20) Zhao, L.; Fan, L. Z.; Zhou, M. Q.; Guan, H.; Qiao, S.; Antonietti, M.; Titirici, M. M. Nitrogen-Containing Hydrothermal Carbons with Superior Performance in Supercapacitors. *Adv. Mater.* **2010**, *22*, 5202.

(21) Li, G.; Zhang, X.; Qiu, D.; Liu, Z.; Yang, C.; Cockreham, C. B.; Wang, B.; Fu, L.; Zhang, J.; Sudduth, B. Tuning Ni/Al Ratio to Enhance Pseudocapacitive Charge Storage Properties of Nickel−Aluminum Layered Double Hydroxide. *Adv. Electron. Mater.* **2019**, *5*, 1900215.

(22) Brezesinski, T.; Wang, J.; Tolbert, S. H.; Dunn, B. Ordered Mesoporous α-MoO3 with Iso-Oriented Nanocrystalline Walls for Thin-Film Pseudocapacitors. *Nat. Mater.* **2010**, *9*, 146.

(23) Liu, X.; Huang, J.; Wei, X.; Yuan, C.; Liu, T.; Cao, D.; Yin, J.; Wang, G. Preparation and Electrochemical Performances of Nanostructured CoxNi1-x(OH)2 Composites for Supercapacitors. *J. Power Sources* **2013**, *240*, 338−343.

(24) Kong, D.; Ren, W.; Cheng, C.; Wang, Y.; Huang, Z.; Yang, H. Y. Three-Dimensional NiCo2O4@Polypyrrole Coaxial Nanowire Arrays on Carbon Textiles for High-Performance Flexible Asymmetric Solid-State Supercapacitor. *ACS Appl. Mater. Interfaces* **2015**, *7*, 21334.

(25) Kim, H. S.; Cook, J. B.; Lin, H.; Ko, J. S.; Tolbert, S. H.; Ozolins, V.; Dunn, B. Oxygen Vacancies Enhance Pseudocapacitive Charge Storage Properties of MoO3-X. *Nat. Mater.* **2017**, *16*, 454.

(26) Ling, T.; Da, P.; Zheng, X.; Ge, B.; Hu, Z.; Wu, M.; Du, X. W.; Hu, W.-B.; Jaroniec, M.; Qiao, S. Z. Atomic-Level Structure Engineering of Metal Oxides for High-Rate Oxygen Intercalation Pseudocapacitance. *Sci. Adv.* **2018**, *4*, eaau6261.

(27) Shao, M.; Ning, F.; Zhao, Y.; Zhao, J.; Wei, M.; Evans, D. G.; Duan, X. Core-Shell Layered Double Hydroxide Microspheres with Tunable Interior Architecture for Supercapacitors. *Chem. Mater.* **2012**, *24*, 1192.

(28) Li, G.; Zhang, X.; Qiu, D.; Liu, Z.; Yang, C.; Cockreham, C. B.; Wang, B.; Fu, L.; Zhang, J.; Sudduth, B. Tuning Ni/Al Ratio to Enhance Pseudocapacitive Charge Storage Properties of Nickel−Aluminum Layered Double Hydroxide. *Adv. Electron. Mater.* **2019**, *5*, 1900215.

(29) Kulkarni, P.; Nataraj, S. K.; Balakrishna, R. G.; Nagaraju, D. H.; Reddy, M. V. Nanostructured Binary and Ternary Metal Sulfides: Synthesis Methods and Their Application in Energy Conversion and Storage Devices. *J. Mater. Chem. A* **2017**, *5*, 22040.

(30) Shen, L.; Yu, L.; Wu, H.-B.; Yu, X. Y.; Zhang, X.; Lou, X. W. Formation of Nickel Cobalt Sulfide Ball-in-Ball Hollow Spheres with Enhanced Electrochemical Pseudocapacitive Properties. *Nat. Commun.* **2015**, *6*, 6694.

(31) Bryan, A. M.; Santino, L. M.; Lu, Y.; Acharya, S.; D'Arcy, J. M. Conducting Polymers for Pseudocapacitive Energy Storage. *Chem. Mater.* **2016**, *28*, 5989.

(32) Xu, H.; Zhao, Y.; Hickmott, D. D.; Lane, N. J.; Vogel, S. C.; Zhang, J.; Daemen, L. L. High-Temperature Neutron Diffraction Study of Deuterated Brucite. *Phys. Chem. Miner.* **2013**, *40* (10), 799−810.

(33) Mishra, G.; Dash, B.; Pandey, S. Layered Double Hydroxides: A Brief Review from Fundamentals to Application as Evolving Biomaterials. *Appl. Clay Sci.* **2018**, *153*, 172.

(34) Hensen, E. J. M.; Smit, B. Why Clays Swell. *J. Phys. Chem. B* **2002**, *106*, 12664.

(35) Gund, G. S.; Dubal, D. P.; Jambure, S. B.; Shinde, S. S.; Lokhande, C. D. Temperature Influence on Morphological Progress of Ni(OH)2 Thin Films and Its Subsequent Effect on Electrochemical Supercapacitive Properties. *J. Mater. Chem. A* **2013**, *1*, 4793.

(36) Wang, L. Y.; Tong, D. S.; Zhao, L. Z.; Liu, F. G.; An, N.; Yu, W. H.; Zhou, C. H. Utilization of Alum Sludge for Producing Aluminum Hydroxide and Layered Double Hydroxide. *Ceram. Int.* **2014**, *40*, 15503.

(37) Navrotsky, A.; Ma, C.; Lilova, K.; Birkner, N. Nanophase Transition Metal Oxides Show Large Thermodynamically Driven Shifts in Oxidation-Reduction Equilibria. *Science* **2010**, *330* (6001), 199−201.

(38) Birkner, N.; Navrotsky, A. Rapidly Reversible Redox Transformation in Nanophase Manganese Oxides at Room Temperature Triggered by Changes in Hydration. *Proc. Natl. Acad. Sci. U. S. A.* **2014**, *111*, 6209.

(39) Birkner, N.; Navrotsky, A. Thermodynamics of Manganese Oxides: Sodium, Potassium, and Calcium Birnessite and Cryptomelane. *Proc. Natl. Acad. Sci. U. S. A.* **2017**, *114*, E1046.

(40) Schneider, C. A.; Rasband, W. S.; Eliceiri, K. W. NIH Image to ImageJ: 25 Years of Image Analysis. *Nat. Methods* **2012**, *9*, 671.

(41) Wu, D.; Hwang, S.-J.; Zones, S. I.; Navrotsky, A. Guest−Host Interactions of a Rigid Organic Molecule in Porous Silica Frameworks. *Proc. Natl. Acad. Sci. U. S. A.* **2014**, *111* (5), 1720−1725.

(42) Wu, L.; Li, L.; Evans, S. F.; Eskander, T. A.; Moyer, B. A.; Hu, Z.; Antonick, P. J.; Harrison, S.; Paranthaman, M. P.; Riman, R. Lithium Aluminum-Layered Double Hydroxide Chlorides (LDH): Formation Enthalpies and Energetics for Lithium Ion Capture. *J. Am. Ceram. Soc.* **2018**, *102* (5), 2398−2404.